

Spatially Resolved Kinematics of SLACS Lenses

SHAWN KNABEL ¹, CHIH-FAN CHEN,¹ TOMMASO TREU,¹
(TDCOSMO)

¹ *University of California, Los Angeles*
Address
Washington, DC 20006, USA

ABSTRACT

AAS Journals, the Astrophysical Journal (ApJ), the Astrophysical Journal Letters (ApJL), the Astronomical Journal (AJ), and the Planetary Science Journal (PSJ) all have a 250 word limit for the abstract^{a)}. If you exceed this length the Editorial office will ask you to shorten it.

Keywords: Galaxies, Galaxy kinematics, Galaxy dynamics

1. INTRODUCTION

The extragalactic Universe contains galaxies of a wide variety of morphologies and features that delineate evolutionary paths through cosmic history. The observational study and classification of these features have led to the forming of powerful empirical relationships like the Fundamental Plane of elliptical galaxies (FP), etc... One of the key insights of the FP is a connection of the dispersion of stellar velocities to the size and brightness of the galaxies. Through dynamical studies, the stellar velocity dispersion traces the mass distribution of the galaxy. Kinematics therefore deservedly holds a distinguished contribution to extragalactic astronomy. Kinematics of external galaxies have historically been observationally lucrative. Kinematics of the structural components of nearby galaxies give insights to the local population and analogous Milky Way studies. Integrated line-of-sight velocity dispersions of external galaxies are possible with single-aperture spectroscopy and have contributed significantly to the characterization of the masses of distant galaxies through dynamical inferences. These kinematics measurements are aperture-integrated and do not contain two-dimensional information necessary for the characterization of rotational velocities. Instead they are a simplistic probe of the typical differences in line-of-sight (or radial) velocities of the measured galaxy components, e.g. stellar or gas. Typically, stellar velocity dispersions are what we can reliably measure. The actual observable quantity is the Doppler broadening of spectral line features due to the dispersion of stellar velocities within the system. The line features, typically stellar absorption lines, are broadened as the line absorption from an individual star with velocity v_k is blue- or red-shifted from the mean wavelength λ , which is itself redshifted due to the expansion of the universe. The observed spectrum is de-redshifted by the galaxy's intrinsic redshift (recession velocity) to its restframe to be compared to a model spectrum, a linear combination of stellar templates. The model spectrum is adjusted by Doppler broadening, and the velocity dispersion that results in the best fit (in a χ^2 sense) is the measurement.

Several decisions in this process introduce systematic uncertainties and biases that need to be accounted. For example, the choice of line features and range of continuum inclusion makes a significant difference to the calculated velocity broadening. Traditionally, the Calcium II H and K stellar absorption lines (3934, 3969Å, hereafter CaHK) have been used to measure kinematics (see e.g. ?). CaHK are very strong and intrinsically broad features, which makes them ideal for detections with low brightness and low S/N. ? found significant bias toward higher velocity dispersions when using CaHK when compared with other line measurements. They suggest that the intrinsic broadness (large equivalent width) and steepness of the surrounding continuum lead to the overestimates. ? suggests that it is most appropriate for galaxies with very large velocity dispersions (> 300 km/s) or low luminosity. Alternative features have

^{a)} Abstracts for Research Notes of the American Astronomical Society (RNAAS) are limited to 150 words

also been used. NaD ($\sim 5900\text{\AA}$) has typically been disfavored due to contamination by the target galaxy’s interstellar gas. Mg I b triplet ($\sim 5200\text{\AA}$) and G-band (CH and Fe, $\sim 4300\text{\AA}$) are complex and fairly weak features compared with CaHK, but they may be more reliable given sufficient resolution. The subject is still under some debate, but CaHK is generally accepted to be a reasonable choice.

Galaxy kinematics studies gained an additional dimension with the advent and now ubiquity of integral-field spectrometers (IFS) on most major observatories (e.g. MUSE, OSIRIS, KCWI). This technology allows for spatially resolved velocity measurements because each spatial pixel (or spaxel) is dispersed into a spectrum. The added spatial information allows the inference of the spatial dependence of the projected kinematic profile. This 2D projection, with dynamical arguments and other physical constraints, can be decoded to describe the 3D stellar orbits, which traces the gravitational potential of the galaxy. The 3-dimensional nature of the stellar orbits encoded in the observable 2D kinematics are described by *anisotropy* parameters, which show how the stellar velocity ellipsoid deviates from an isotropic case. In many cases, this anisotropy can be summarized as a single parameter

$$\beta_{ani}(\mathbf{r}) \equiv 1 - \frac{\sigma_t(\mathbf{r})^2}{\sigma_r(\mathbf{r})^2}$$

where σ_t and σ_r are the tangential and radial velocity dispersions, respectively, so that $\beta_{ani} = 0$ corresponds to an isotropic case (spherically velocity ellipsoid). The 2D kinematic profile, in the form of binned kinematic maps, shows the degree of rotational, orderly, and random velocities of stellar orbits.

These IFS kinematics studies have opened new galaxy-classification schemes and offered insights to the formation mechanisms of elliptical galaxies (see for a full review ?). Morphological classification of galaxies classically led to formation and evolution theories that connected disk galaxies with younger stellar populations and more mature elliptical galaxies with more random stellar orbits. The mechanisms by which a galaxy may evolve along this axis included dry collisional merging of galaxies or by the self-quenching of stellar activity by some internal processes. Observationally, large surveys have compared the visual morphology and kinematic information to discover that the binary classification is far too simple to adequately describe the entire population of galaxies. In fact, the parameter space of features that describe younger disk galaxies and their elliptical cousins overlaps between the two considerably. Many galaxies that appear to be elliptical are actually disky structures that rotate regularly. They feature older stellar populations than nearby disk galaxies and appear therefore to be formed through a relatively mergerless life cycle. The cases that resemble the more classic elliptical picture, with almost no regular rotation and triaxial structure, are likely the result of mergers. These have been termed “fast- and slow-rotators,” as they can be distinctly classified with significantly different kinematic attributes.

Dynamical models of elliptical galaxies have been created using solutions to the two- and three-integral Jeans equations of stellar hydrodynamics in axisymmetric and spherical alignments with detailed 2D kinematic maps, and more generally with Schwarzschild models of orbital superposition and (what was the other one in Cappellari?). Dynamical mass models of massive elliptical galaxies have been shown to be in excellent agreement with lensing measurements, and joint constraints between the two methods have been used to precisely determine mass profiles and overcome the problematic mass-sheet degeneracy associated with lens modeling. Line-of-sight velocity dispersions from single-slit spectroscopy can constrain galaxy dynamics, but there exists another pesky degeneracy, the mass-anisotropy degeneracy (MAD), which cannot be broken without spatial resolved kinematics. By breaking the elliptical galaxy mass-anisotropy degeneracy, one may then be positioned to break the MST.

We present spatially-resolved kinematics of a selection of 14 strong-lensing elliptical galaxies from the well-studied Sloan Lens ACS (SLACS) catalog. Recent lensing models have been conducted in a uniform manner for each, and dynamical models will be presented in a companion to this paper. Observations are taken with the Keck Cosmic Web Imager (KCWI) and will be presented in Section 2. Kinematic analysis methods will be described in Section 3. Systematics and error budgets are discussed in Section 4. Final results and kinematic maps are presented in 5.

2. OBSERVATIONS

We use stellar kinematics from IFS spectroscopy taken with the Keck Cosmic Webb Imager (KCWI) on Keck 2 during both 2021 semesters and the first semester of 2022 (May 6 and 15, June 7, August 12, November 26, 2021; April 7, 2022). We take a series of 30 minute exposures with the blue grating centered at 4600\AA with the small slicer and 1x1 binning. At redshifts around $z \sim 0.2$, sufficient S/N of ~ 20 can be achieved with 2-3 hours of exposure. This places the redshifted CaHK lines well within the observed wavelength range ($3500\text{--}5600\text{\AA}$). NaD and Mg I b lines will

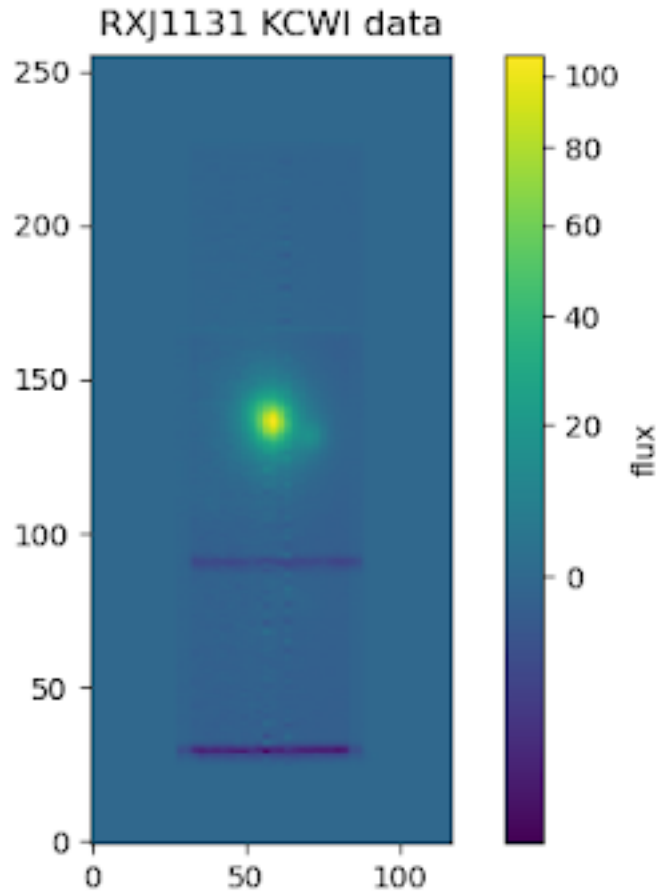


Figure 1. Example of a KCWI datacube mosaic. J0037.

be redshifted beyond 5600\AA for all objects ($z \sim 0.15 - 0.35$). G-band absorption due to CH and neutral Fe ($\sim 4300\text{\AA}$) is observable for some, but not all, targets. For these reasons, we focus on the CaHK absorption features and mask G-band absorption. We dither by 8-ish degrees along the long axis of the IFU field. The resulting 4-5 datacubes are reduced with the KCWI pipeline, and mosaics are created from the frames. An example of one such mosaic is given in Figure 1.

3. KINEMATICS ANALYSIS

The spatially-resolved kinematics analysis is done with python packages developed by Michele Cappellari. Kinematics are measured for an individual spectrum with Cappellari's python implementation of Penalized Pixel-Fitting (PPXF, Cappellari2004, cappellari17), which extracts stellar kinematics by fitting the observed spectrum with a linear combination of stellar spectra convolved with (broadened by) a line of sight velocity distribution constructed with a Gauss-Hermite parametrization. The fit is improved with additive and multiplicative Legendre polynomials. Additive polynomials give greater fitting power by adjusting the strength of individual absorption lines, while multiplicative polynomials minimize the effects of inaccurate spectral calibrations and dust reddening. Line of sight velocity distributions of galaxies have been shown to be well-described with Gaussians, so PPXF penalizes LOSVD fits that deviate from a Gaussian form without improving the fit. See Cappellari17 for a full description.

In our method, the first step fits an aperture-integrated central spectrum from the observational data with a linear combination of stellar templates from a chosen stellar library at wavelengths around the CaH&K absorption lines ($\lambda\lambda 3934, 3969$). The central spectrum fit becomes the global galaxy template spectrum for fitting the other spatial

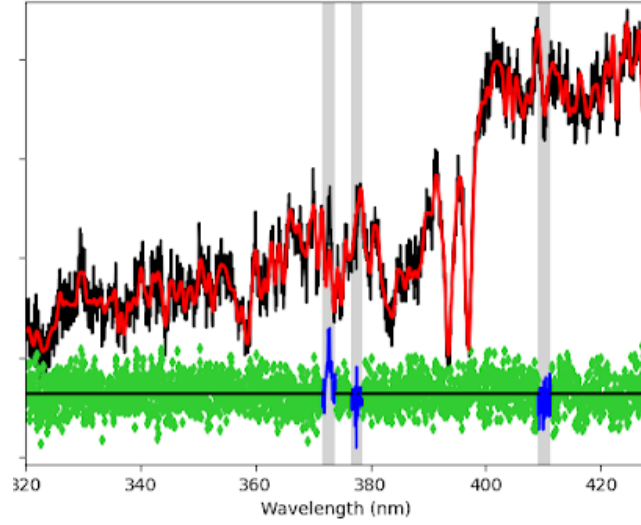


Figure 2. Central deflector galaxy spectrum of J0037 taken with $R=1$, which serves as the global galaxy template spectrum that is fit to each bin.

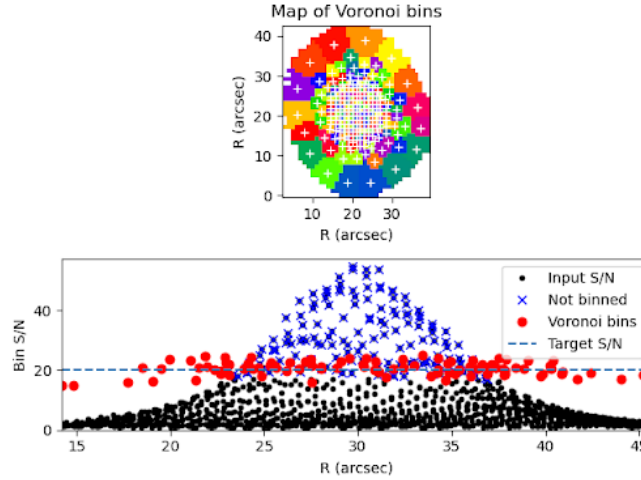


Figure 3. Voronoi binning of J0037.

bins of the datacube. An example global template spectrum is shown in Figure 2. In principle, kinematics can be measured for each spaxel in the datacube by fitting the spaxel spectrum with the global template spectrum. Spaxels at larger radii from the center of the galaxy will suffer from lower S/N than the central spaxels, so they must be binned in order to measure kinematics at a consistent S/N. We use VORBIN Voronoi binning software to select only pixels with S/N greater than 1 and group those pixels to achieve a designated target S/N within each bin (10-20ish). This selection is shown in Figure 3. The composite spectra in each bin are fit with the global galaxy template by convolving with a correction to the global galaxy template LOSVD. The mean velocity is a small correction to the bulk velocity and is subtracted to show the rotation of the galaxy. The result is a pair of kinematic maps that describe the 2D projection of stellar motion within the galaxy, which we show in Figure 4.

4. SYSTEMATICS AND ERROR BUDGET

We test for systematic errors by performing the modeling with 3 selections each of varying stellar spectrum template library, additive polynomial degree, wavelength range, and central spectrum fit aperture size. The stellar spectrum

template library is composed of G and K giants from the X-shooter Spectral Library (Chen2011) by searching the VizieR database for X-shooter stellar atmospheric parameters (Arentsen2019). We take stars with $0.15 < \log g < 3.59$, $-2.5 < \text{Fe/K} < 0.34$, and $4400K < T_{eff} < 5000K$. We test two other temperature ranges to account for slightly hotter and cooler stars, with temperature ranges $4300K < T_{eff} < 5000K$ and $4400K < T_{eff} < 5100K$. Much hotter stars will be thermally broadened instead of kinematically broadened, which will bias the answer. Colder stars are generally not present because the stellar populations are not old enough. For the additive Legendre polynomial we take degrees of 4, 5, and 6. These are appropriate degrees for fitting wavelength ranges of about 1000 \AA . Because the observed spectra are dense with lines, the truncation of any line feature by wavelength boundaries could affect the kinematic fit. To mitigate this effect, our baseline wavelength range is $3200 - 4300 \text{ \AA}$ (leaving plenty of room for CaHK, and we test for narrower ($3250 - 4250 \text{ \AA}$) and wider ($3150 - 4350 \text{ \AA}$) ranges. One exception is made for SDSSJ0330-0020 to avoid a sudden dropoff of flux above 4150 \AA . Upper wavelengths are 4100 , 4050 , and 4150 \AA for this object's fit. Finally, we test the effect of the central aperture size for fitting the global template spectrum. We take pixel-radii of 0, 1, and 2 about the brightest pixel in the foreground galaxy, which takes areas of 1 pixel, 5 pixels, and 9 pixels. Each of these different "solutions" introduces uncertainty for each bin. We marginalize over these systematics, assuming a Gaussian form, by summing each solution weighted by the likelihood $\exp[-\chi^2/2]$. For each n of N bins and k possible solutions, $\sigma_n = \Sigma_k \text{Gaussian}(\mu_k, \sigma_k) \times \exp[-\chi^2/2]$. We produce an $N \times N$ covariance matrix to account for correlation between spatial bins and quantify the full uncertainty in each kinematic map. Systematic errors should account for the large majority of uncertainty.

5. RESULTS

We present the final kinematic maps and uncertainties in Figures 4 and 5.

6. KINEMATIC CLASSIFICATION

Hints of the dichotomy of two main classes of elliptical galaxy were evident even before spatially resolved kinematics were possible, when velocities much lower than theoretical predictions were measured in the first elliptical galaxy stellar kinematics observations (Bertola and Capaccioli 1975, Illingworth 1977; Schechter and Gunn 1979). This challenged the assumption of homogeneous isotropic systems. To quantify this, Binney1978 introduced the $(V/\sigma, \epsilon)$ diagram. V/σ is the ratio of rotational to random velocity integrated spatially across the galaxy, and ϵ is the observed ellipticity of the galaxy. This can be extended to spatially resolved kinematics by taking the flux-weighted average of binned velocities k (cappellari07).

$$\frac{\langle V^2 \rangle}{\langle \sigma^2 \rangle} \approx \frac{\Sigma_k F_k V_k^2}{\Sigma_k F_k \sigma_k^2}$$

This does not actually utilize the spatially information of the kinematic map, so a more quantitative kinematic description can be taken using a parameter $\lambda_{Re} \dots$

Hi Tommaso. :)

I acknowledge myself for hard work.

Facilities: HST(STIS), Swift(XRT and UVOT), AAVSO, CTIO:1.3m, CTIO:1.5m,CXO

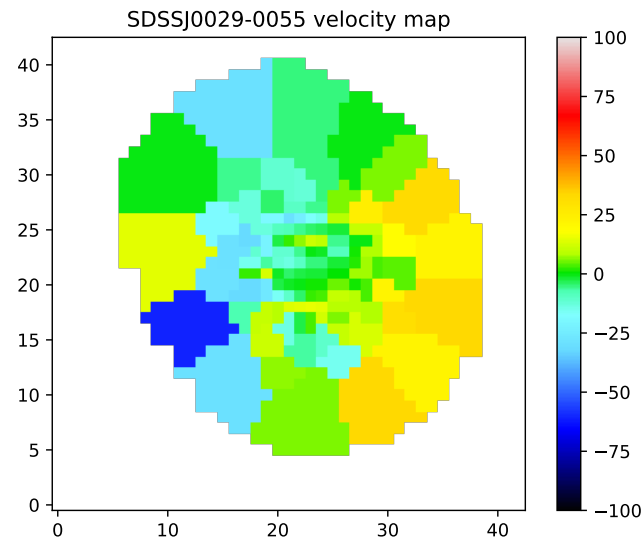
Software: astropy (Astropy Collaboration et al. 2013, 2018), Cloudy (Ferland et al. 2013), Source Extractor (Bertin & Arnouts 1996)

APPENDIX

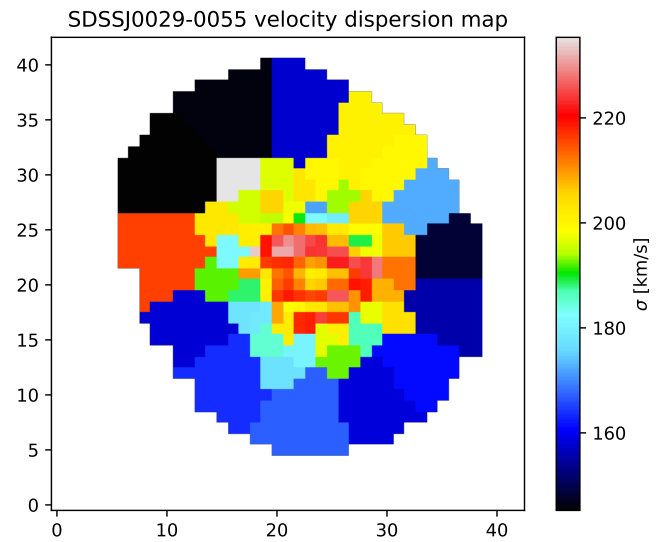
A. APPENDIX INFORMATION

REFERENCES

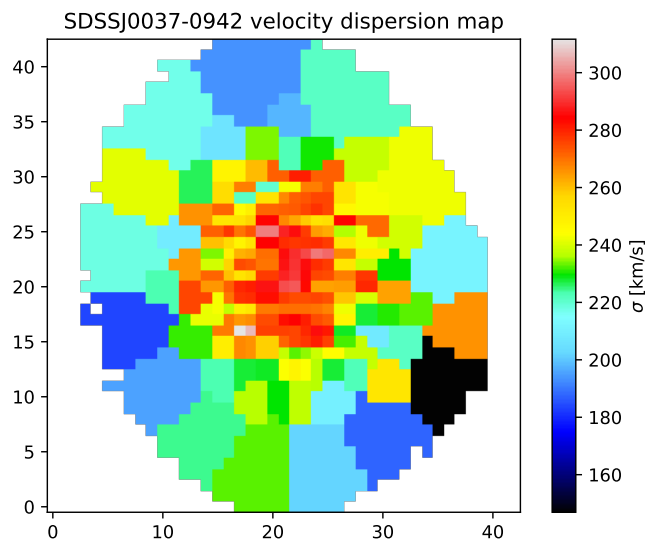
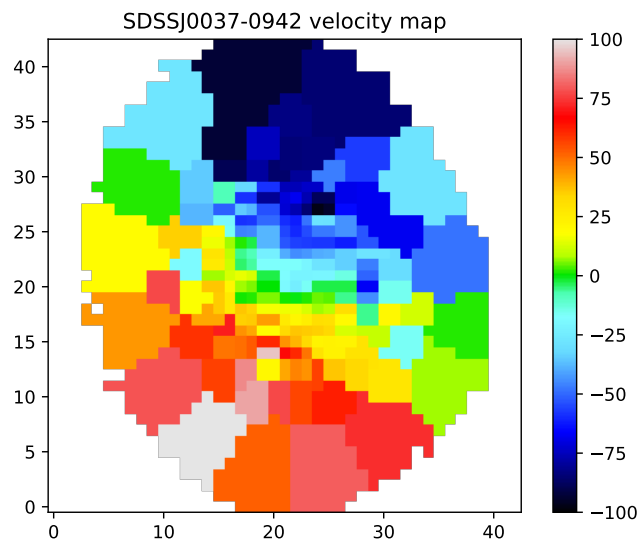
- | | |
|--|--|
| <p>147 Astropy Collaboration, Robitaille, T. P., Tollerud, E. J.,
 148 et al. 2013, A&A, 558, A33,
 149 doi: 10.1051/0004-6361/201322068</p> | <p>150 Astropy Collaboration, Price-Whelan, A. M., Sipőcz, B. M.,
 151 et al. 2018, AJ, 156, 123, doi: 10.3847/1538-3881/aabc4f</p> |
|--|--|



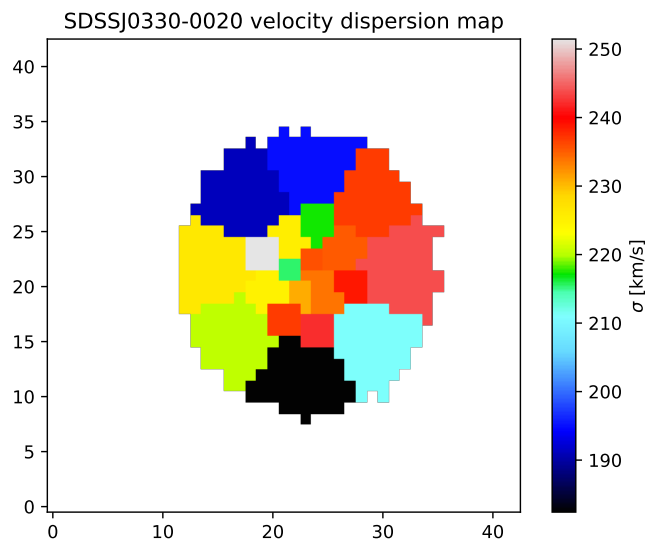
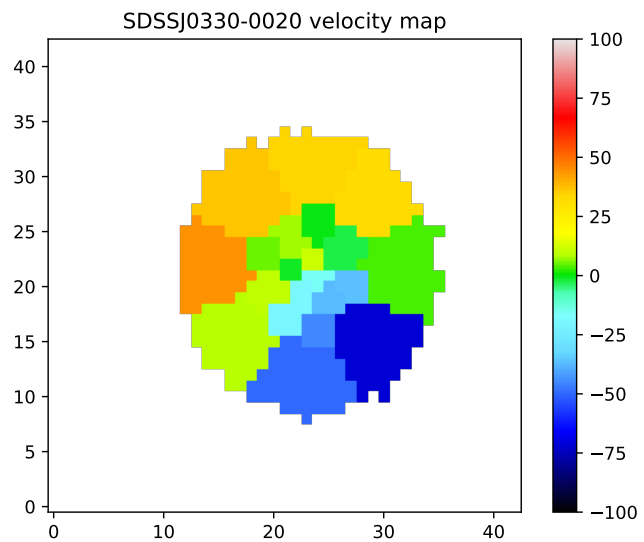
(a)

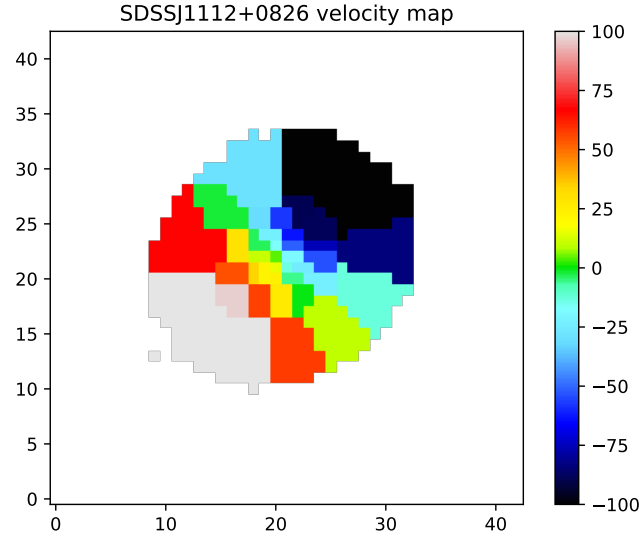


(b)

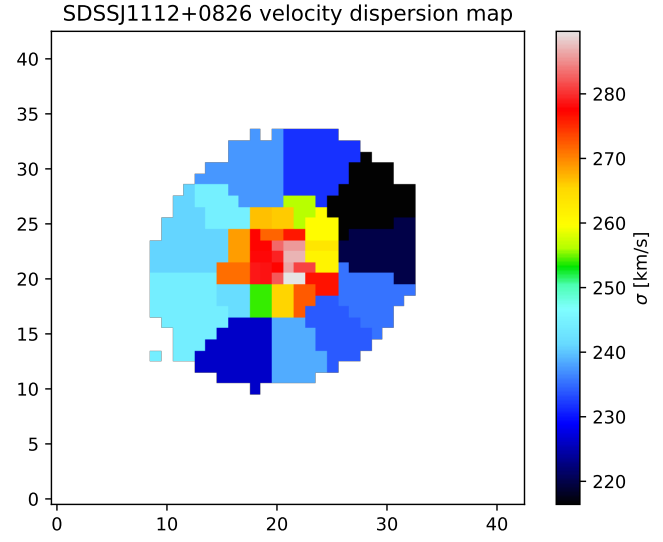


(c)

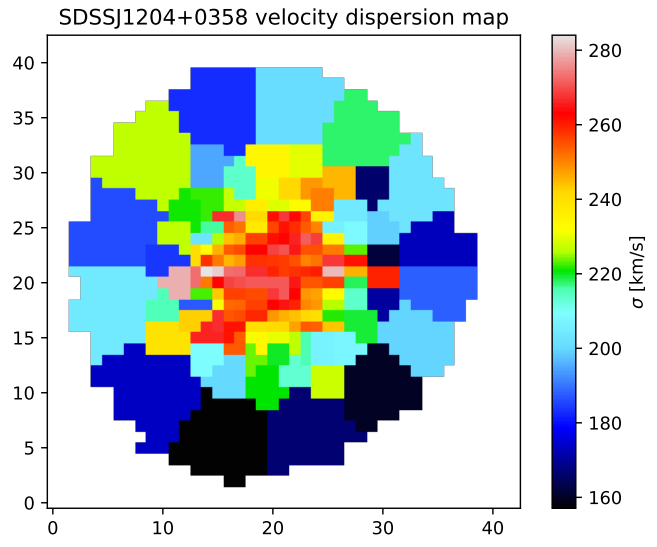
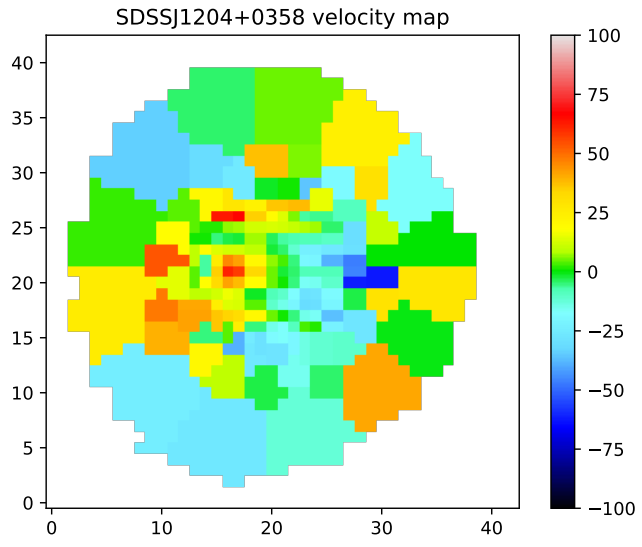




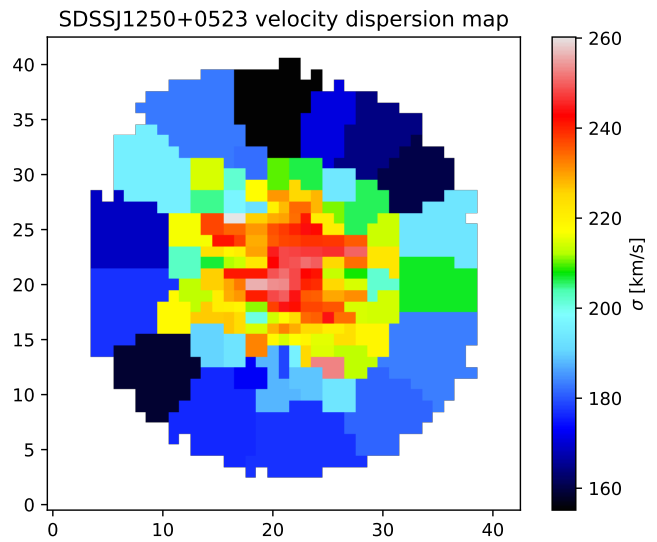
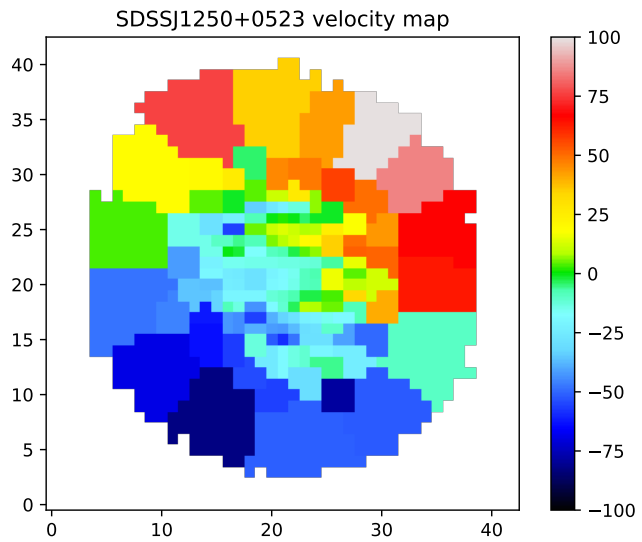
(d)

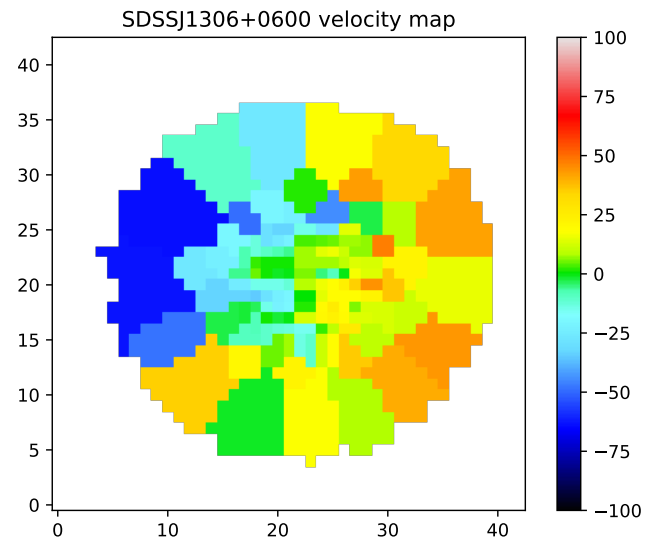


(e)

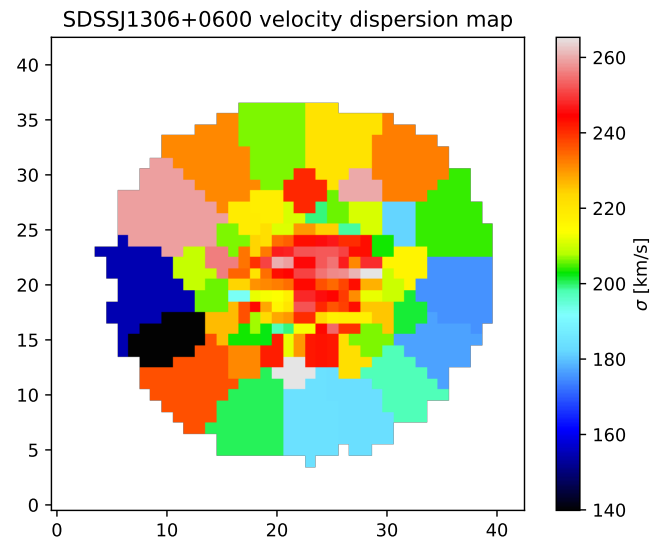


(f)

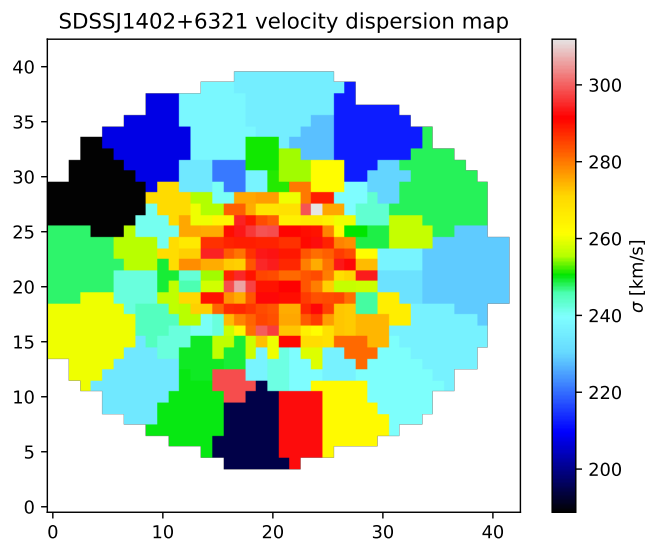
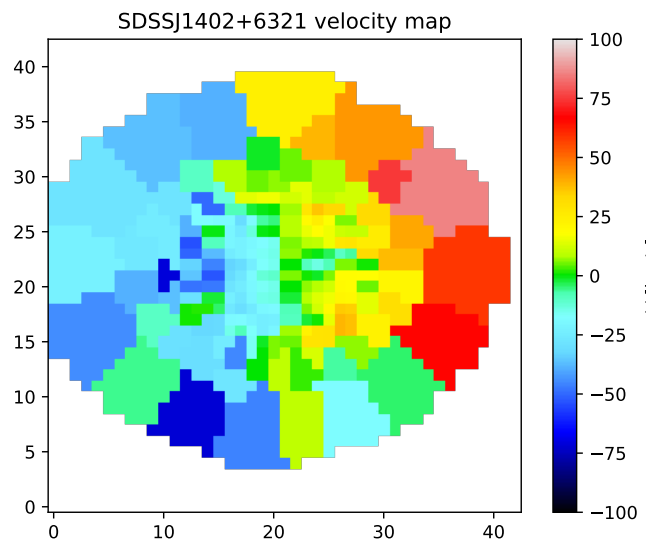




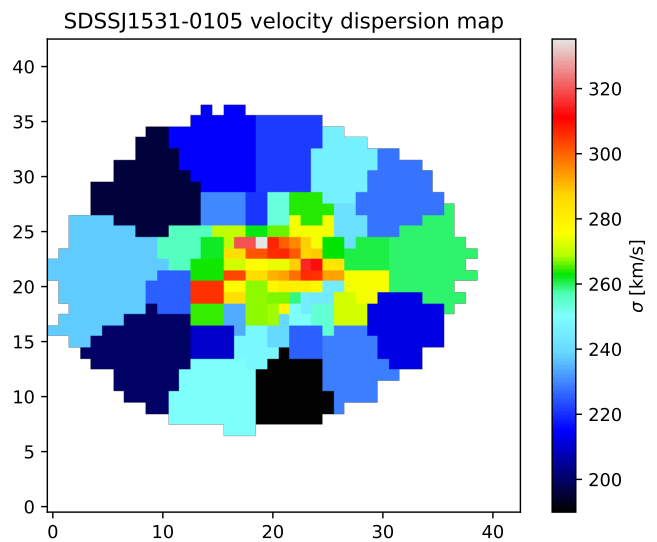
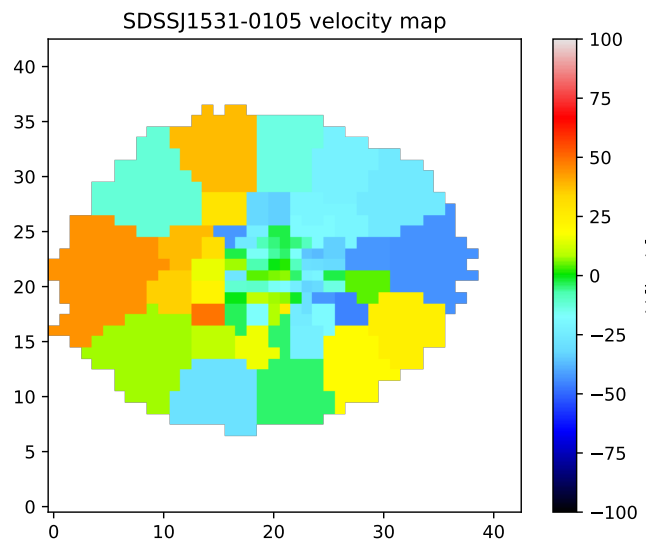
(g)

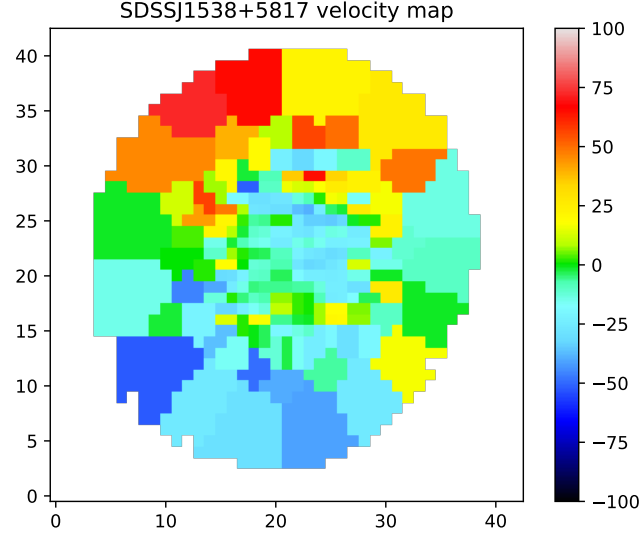


(h)

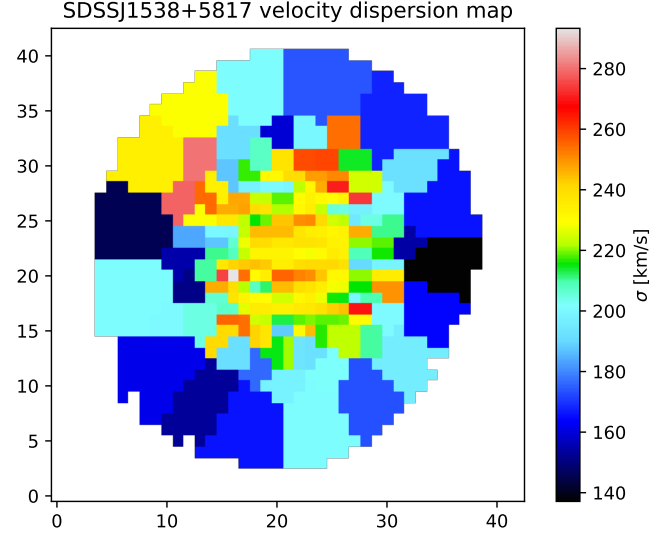


(i)

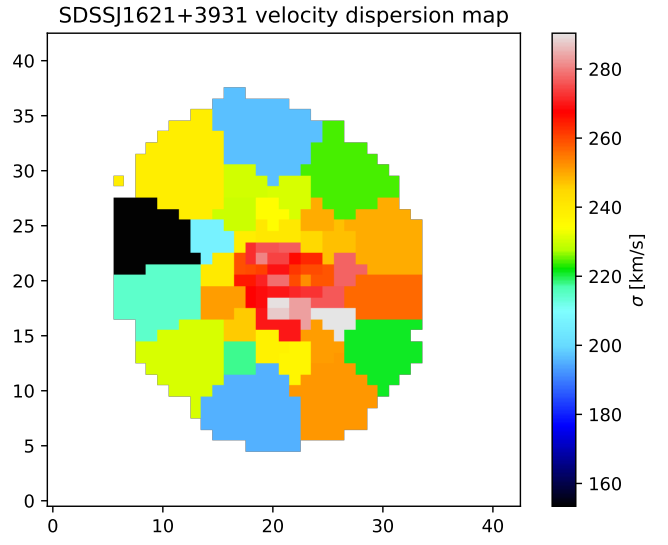
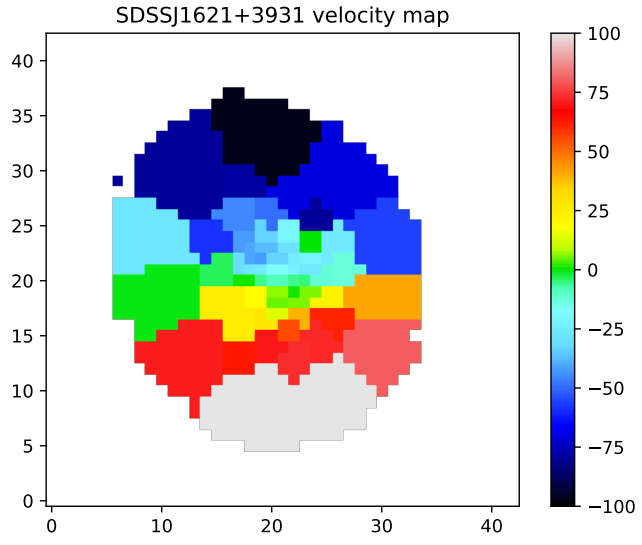




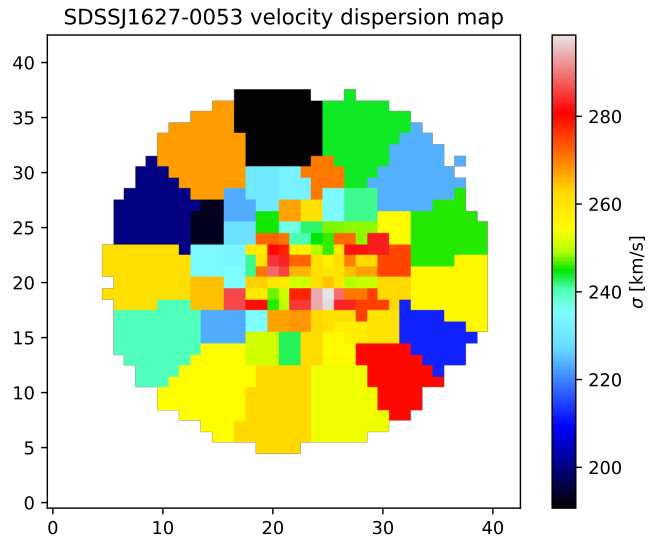
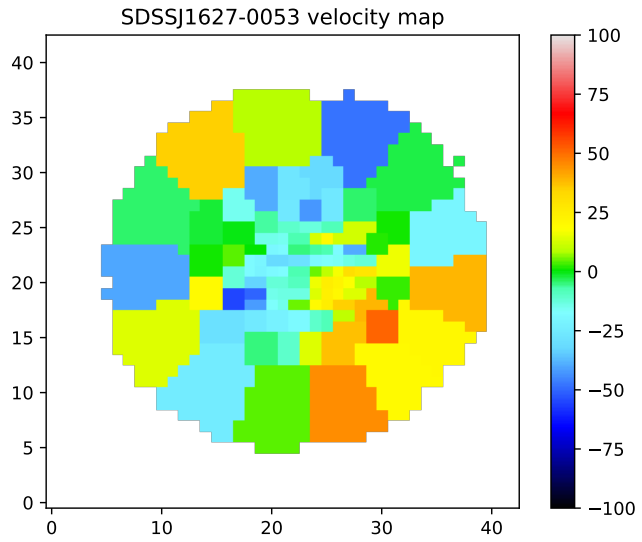
(j)

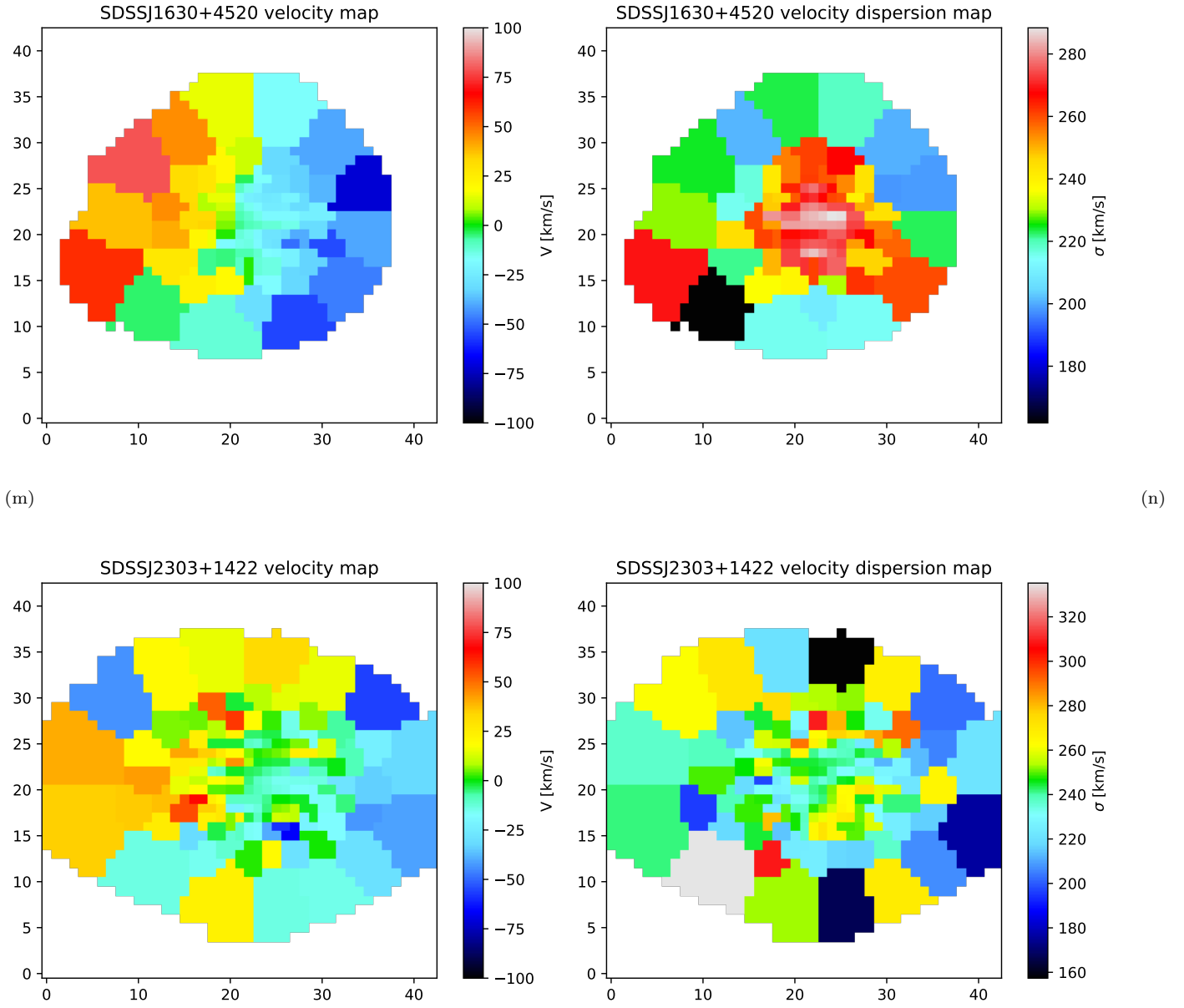


(k)



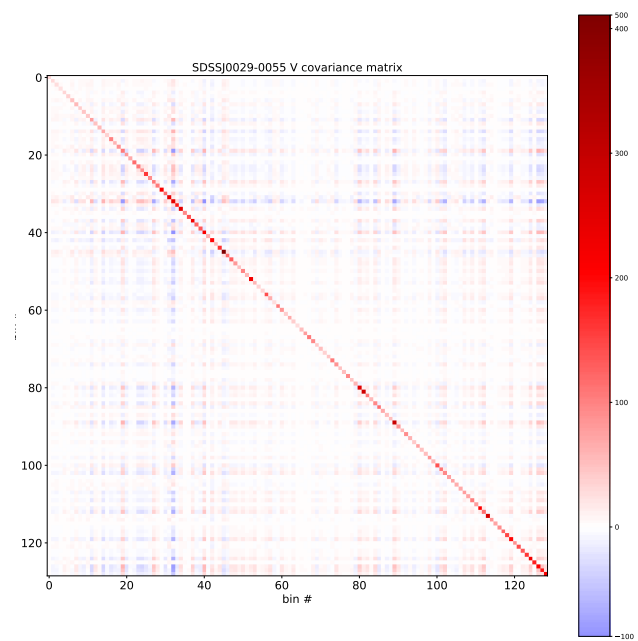
(l)



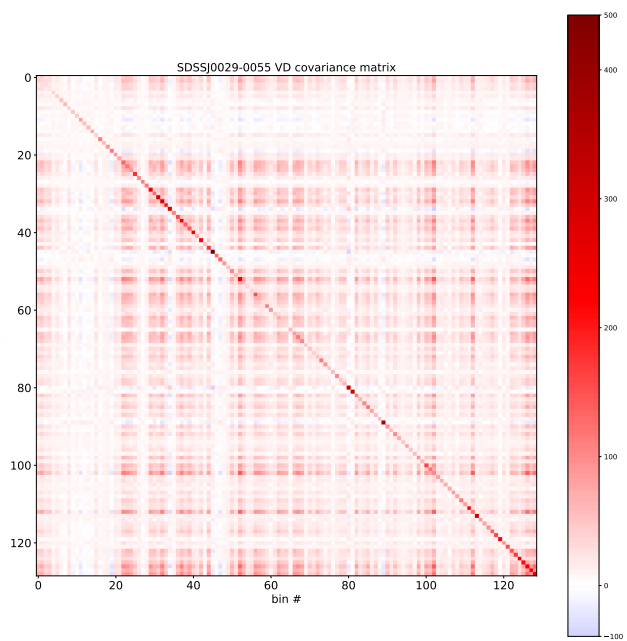
**Figure 4.**

152 Bertin, E., & Arnouts, S. 1996, A&AS, 117, 393,
 153 doi: [10.1051/aas:1996164](https://doi.org/10.1051/aas:1996164)

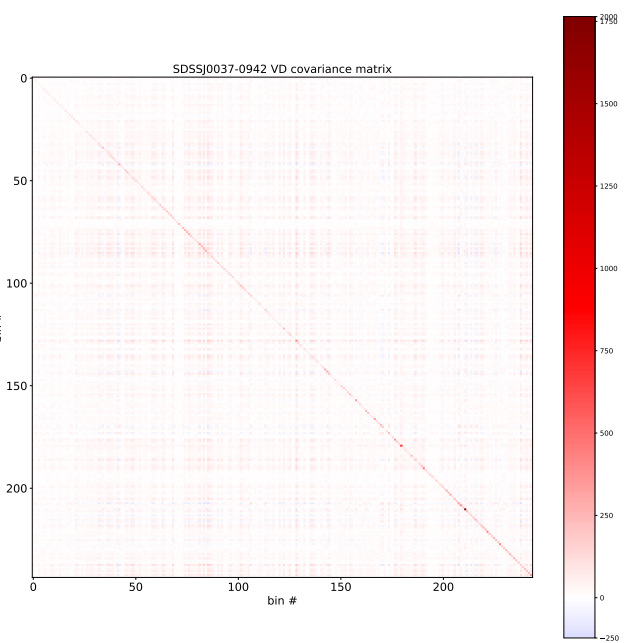
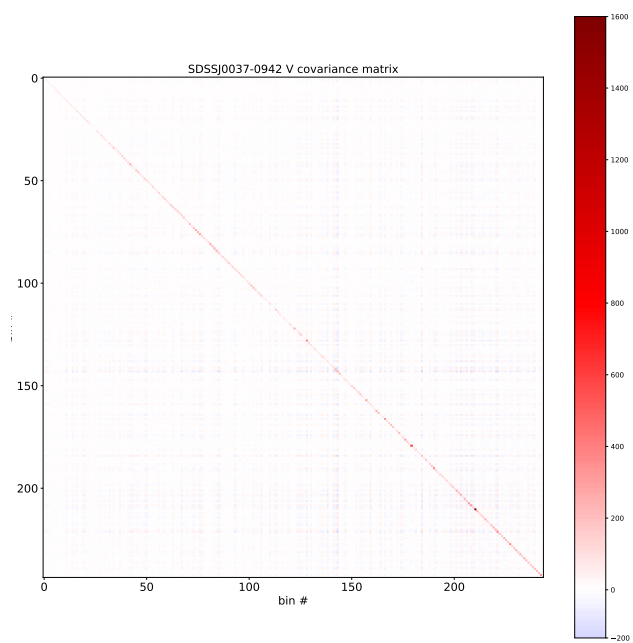
154 Ferland, G. J., Porter, R. L., van Hoof, P. A. M., et al.
 155 2013, RMxAA, 49, 137. <https://arxiv.org/abs/1302.4485>

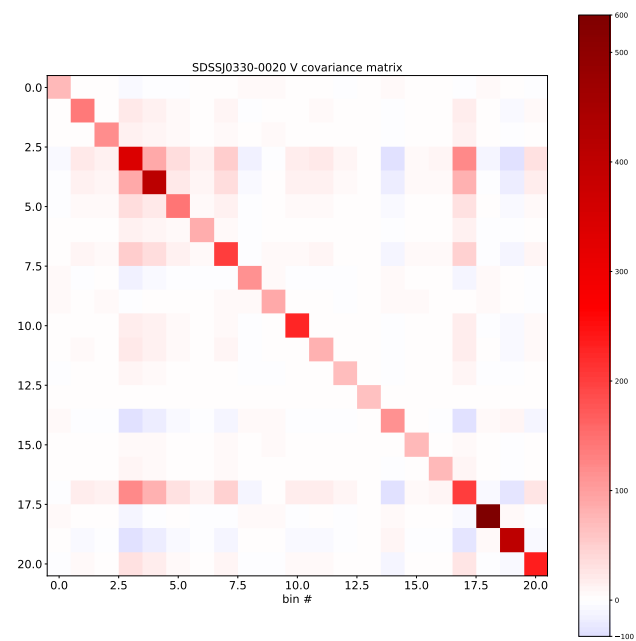


(a)

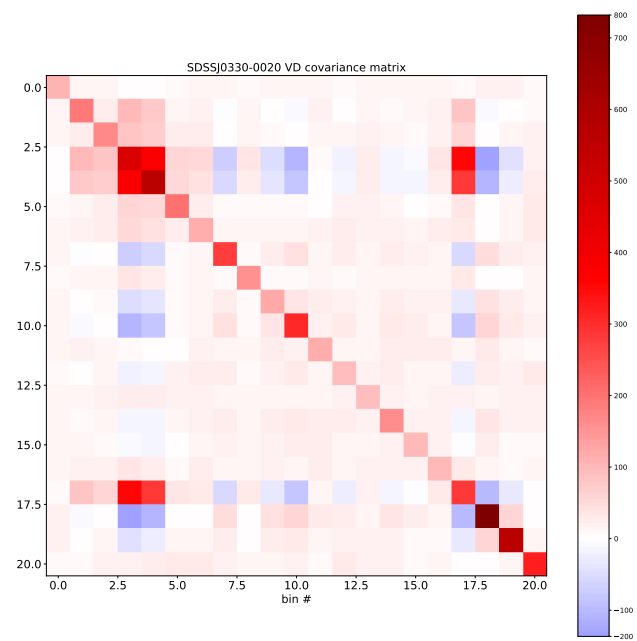


(b)

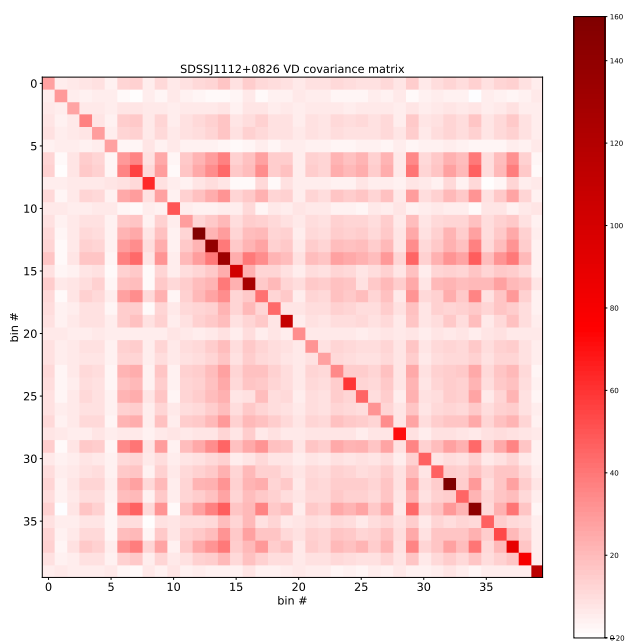
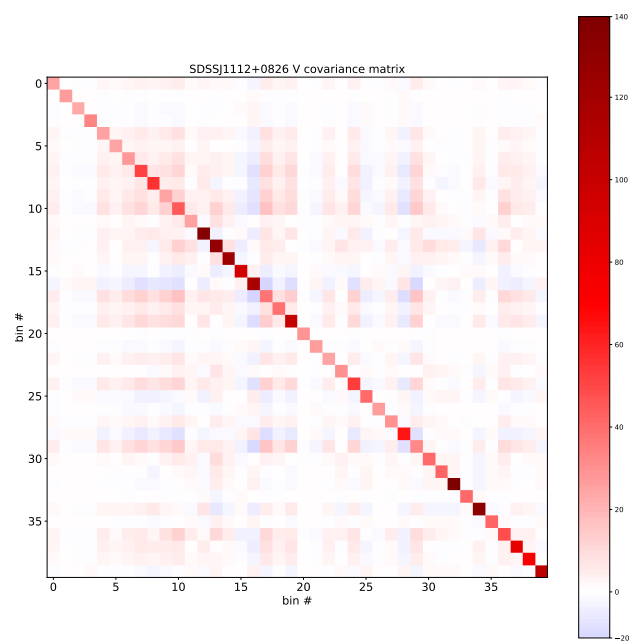


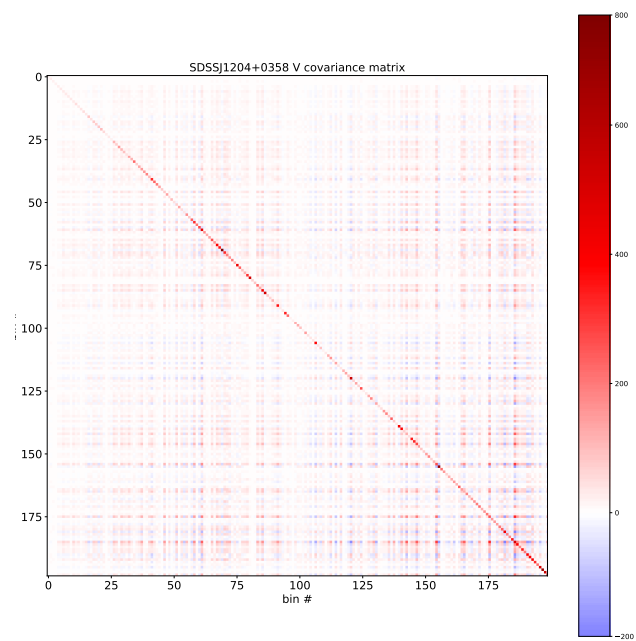


(c)

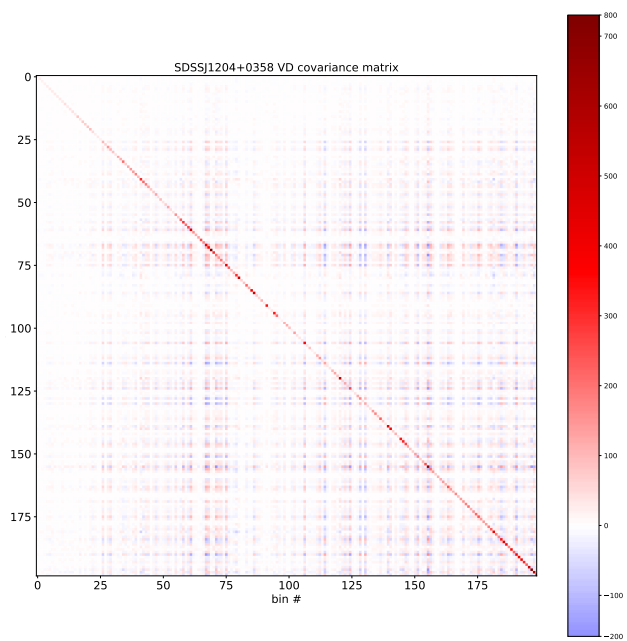


(d)

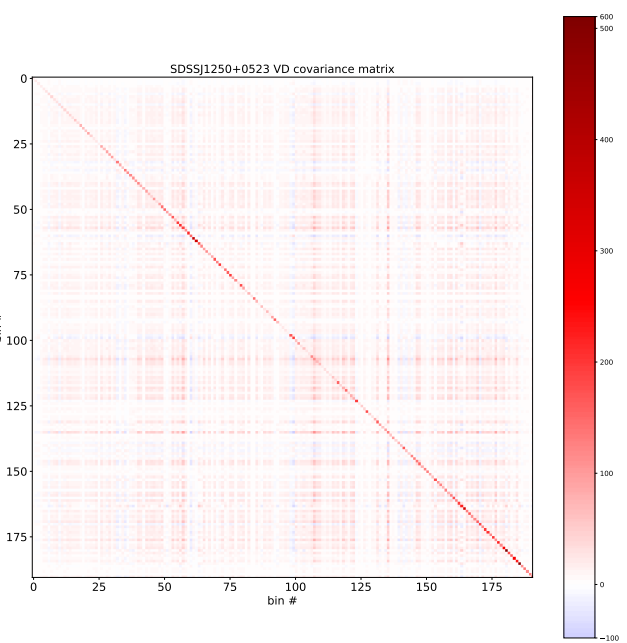
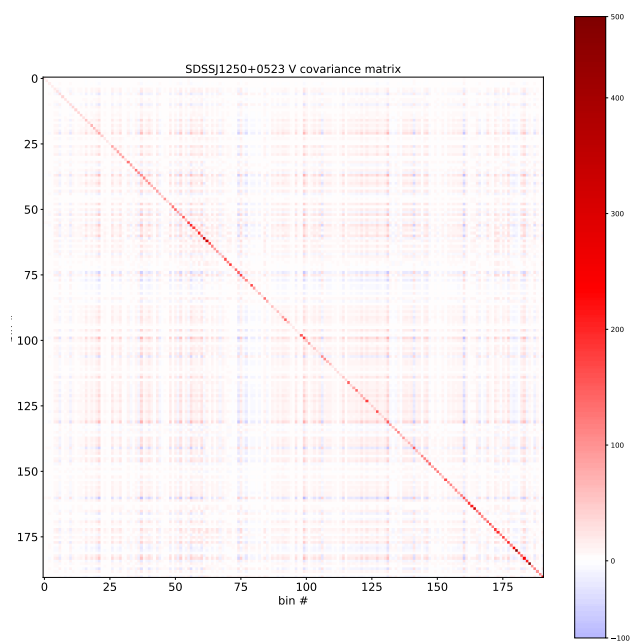


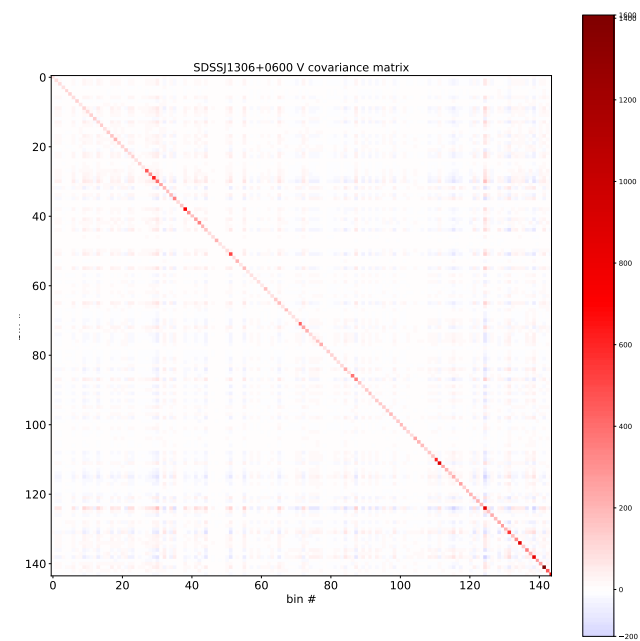


(e)

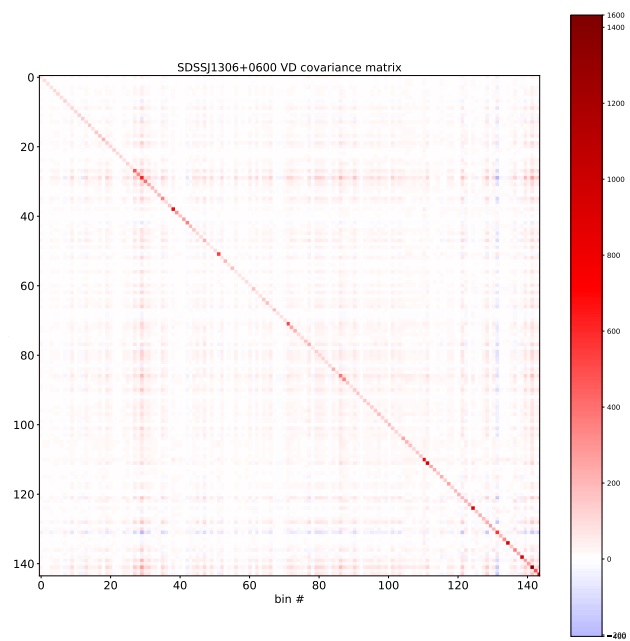


(f)

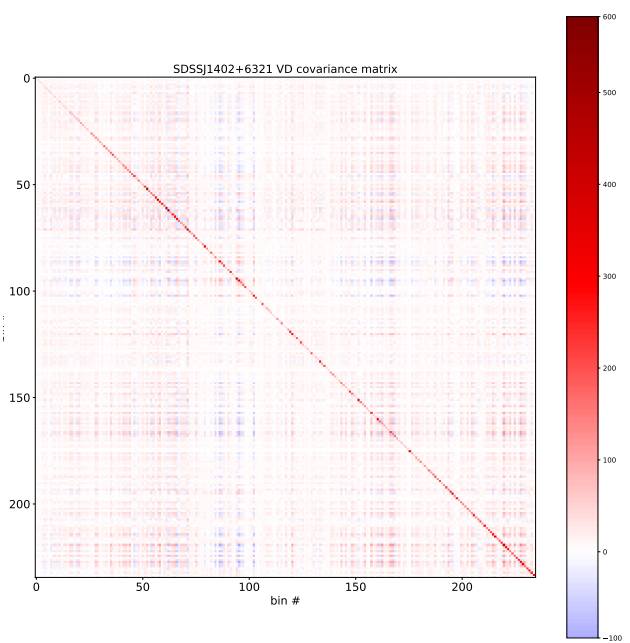
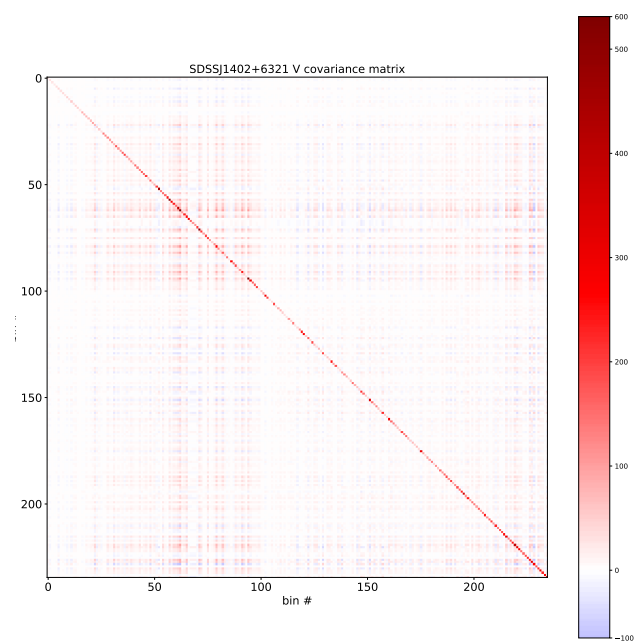


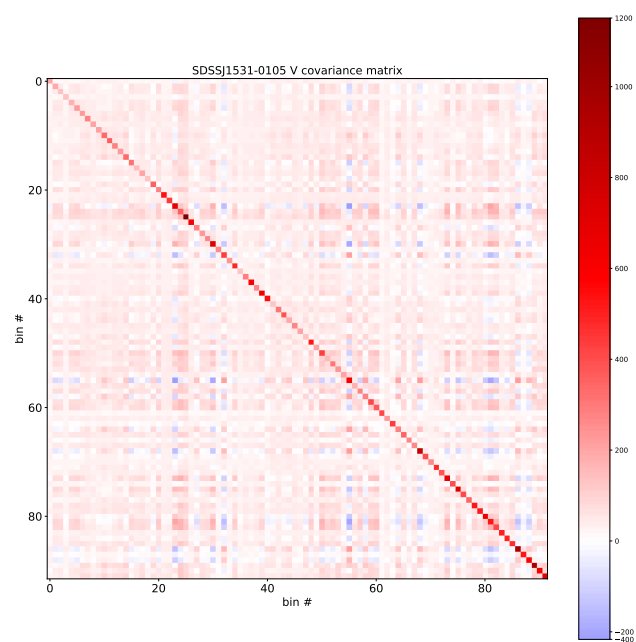


(g)

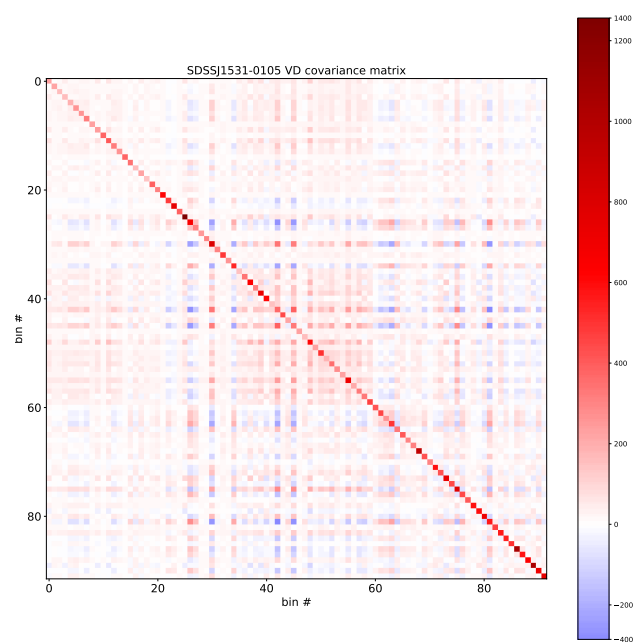


(h)

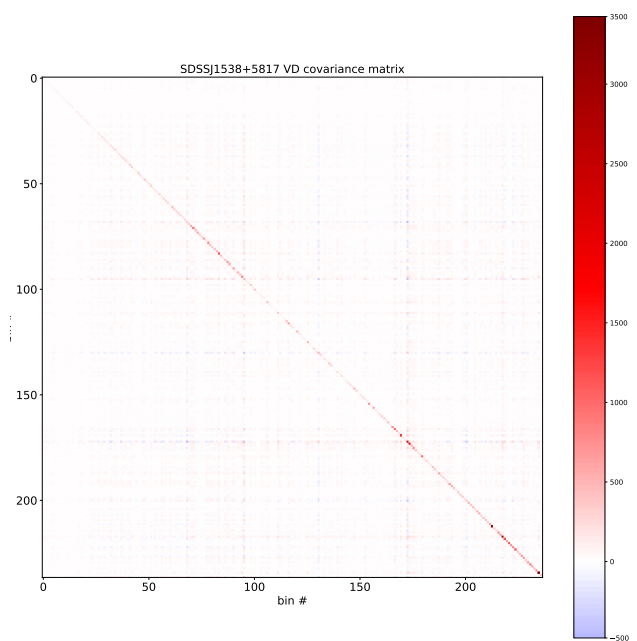
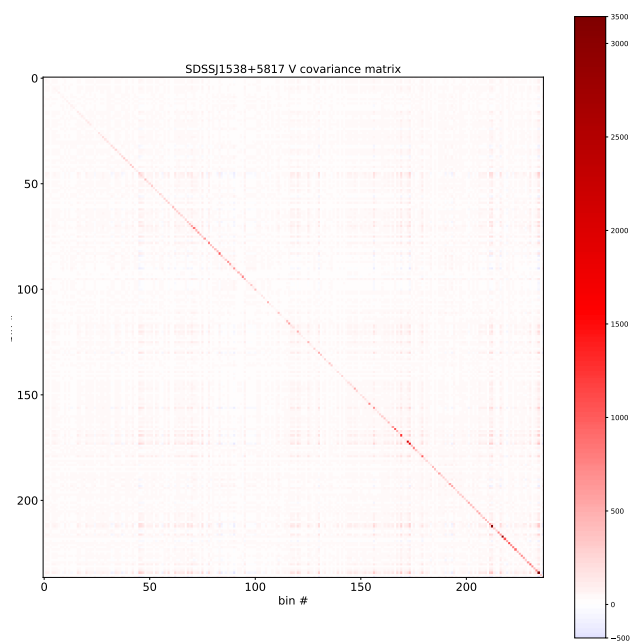


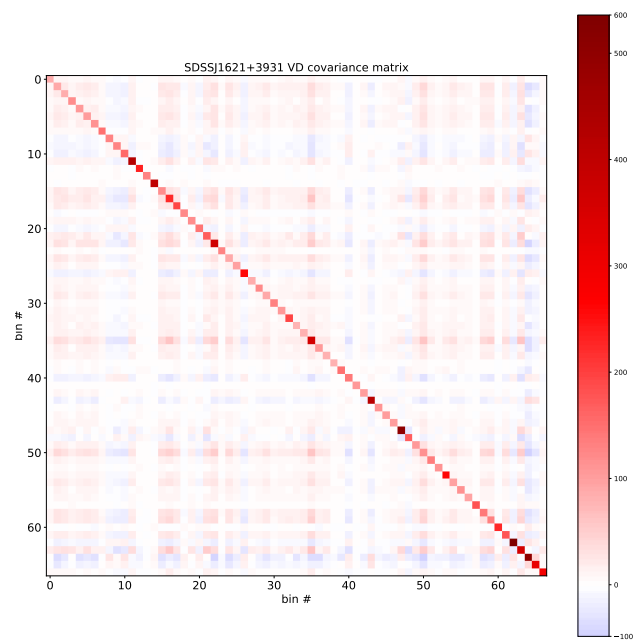
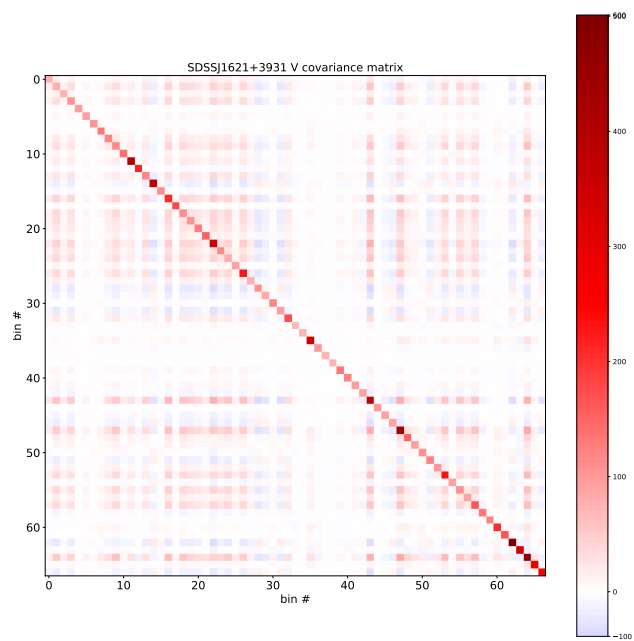


(i)



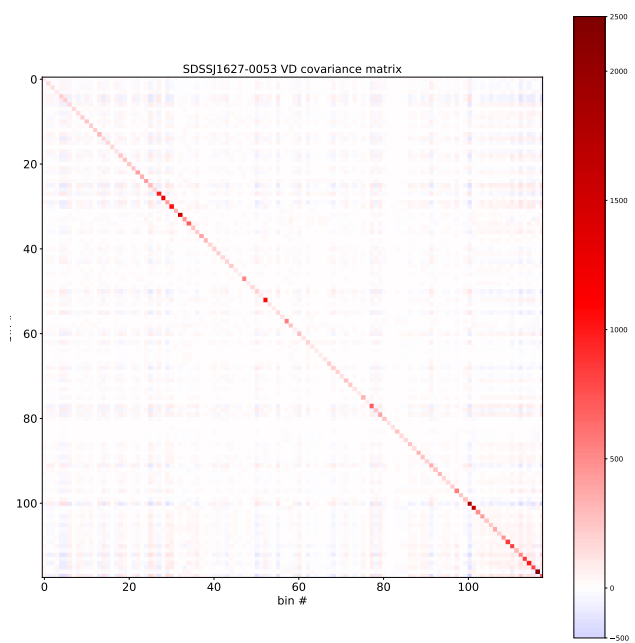
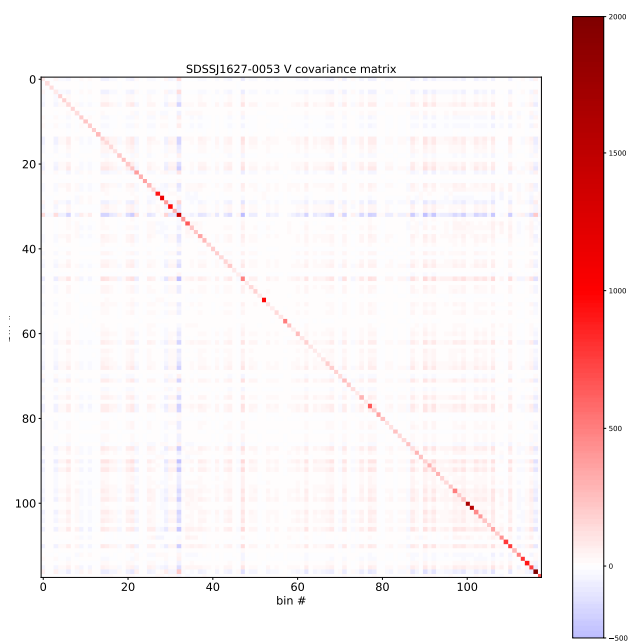
(j)

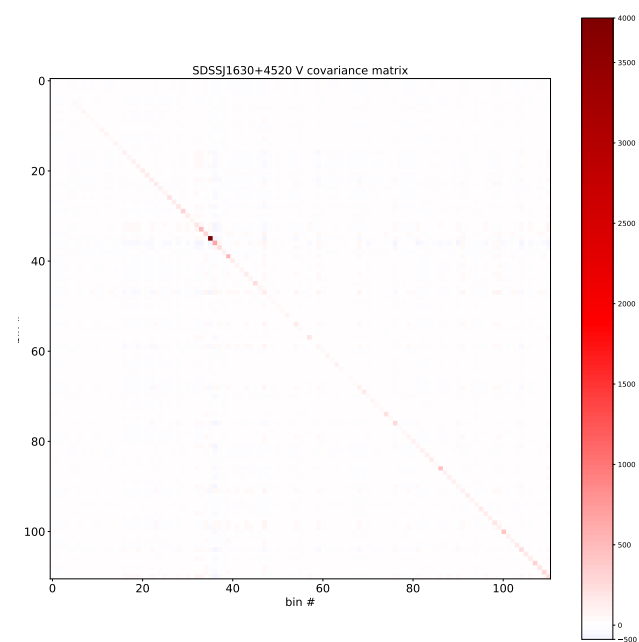




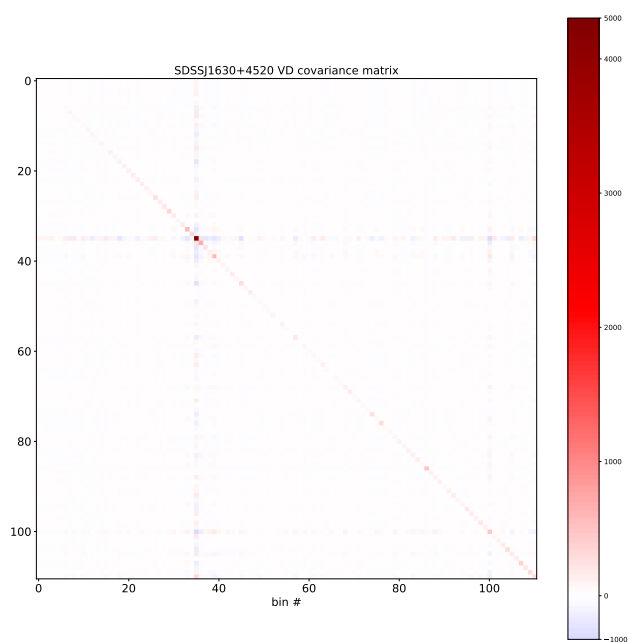
(k)

(l)





(m)



(n)

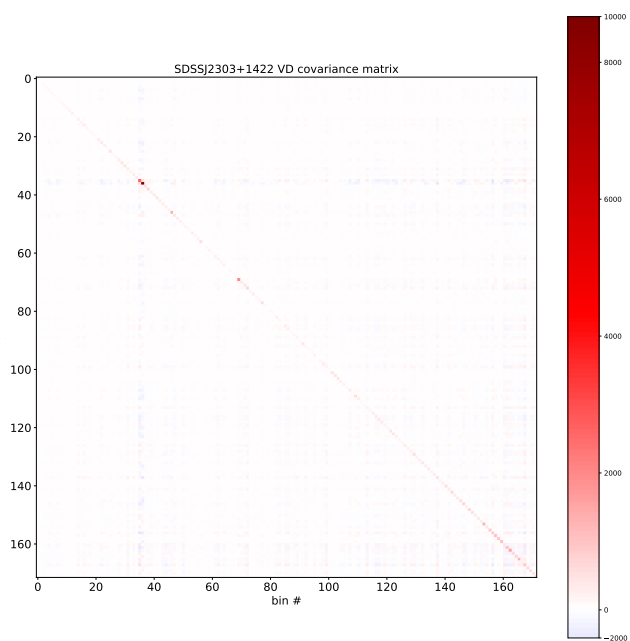
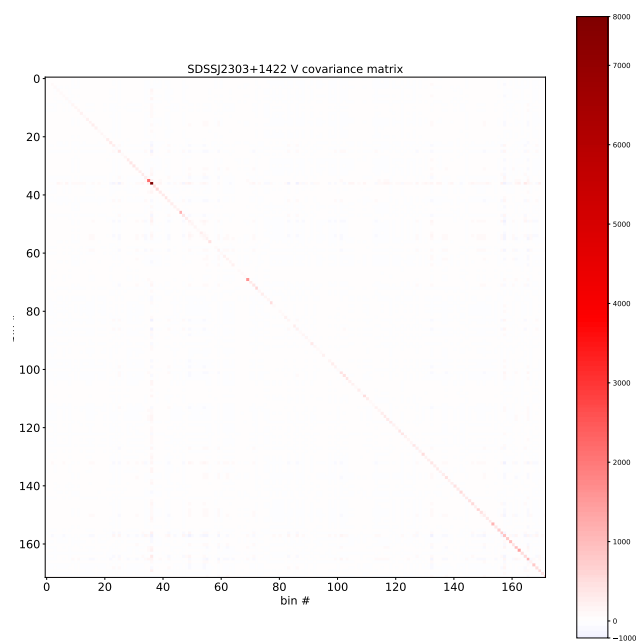


Figure 5.